Manuscript

Influence of SLM scan-speed on microstructure, precipitation of Al₃Sc particles and mechanical properties in Sc- and Zr-modified Al-Mg alloys

A.B. Spierings[1], K. Dawson[2], P.J. Uggowitzer[3], K. Wegener[4]

[1] Innovation Centre for Additive Manufacturing, INSPIRE-AG, Lerchenfeldstrasse 3, CH-9014 St.Gallen, Switzerland
[2] Centre for Materials and Structures, School of Engineering, University of Liverpool, Liverpool L69 3GH, UK
[3] Metal Physics and Technology, Department of Materials, ETH Zurich, CH-8093 Zurich, Switzerland
[4] Institute of Machine Tools and Manufacturing, Department of Mechanical and Process Engineering, ETH Zurich, CH-8092 Zurich, Switzerland

Corresponding author: A.B. Spierings, inspire-AG, spierings@inspire.ethz.ch

_____

Abstract

Additive processing via Selective Laser Melting (SLM) of Sc- and Zr-modified Al-Mg alloys (commercially known as Scalmalloy®) provides significant advantages over traditional 4xxx casting alloys. This is due to the high strength and ductility at very low mechanical anisotropy, which is a result of the alloys' very fine-grained microstructure combined with weak texture in the build-up direction. Next to their advantageous mechanical properties, the reliability of alloys processed by additive manufacturing is of great importance. Variations in microstructural features due to the use of different in processing parameters (e.g. laser scan speed) are well known for traditional alloys. This study analyses the influence of varying laser scan speeds on the static mechanical properties of SLM-processed Scalmalloy®, and discusses the evolving microstructure and precipitation of nm-sized Al₃Sc particles at the correspondingly different energy inputs. It is found that by about doubling the laser scan speed the peak grain sizes in the fine-grained regions decrease from 1.1μm to 600nm, whereas in the coarse grained region almost no influence is observed. Al₃Sc particles are only precipitated during processing at low scan speeds due to the corresponding high laser energy input, or by the intrinsic heat treatment from subsequent layers being built.

Keywords: Selective Laser Melting, Aluminium, TEM, precipitates

1 Introduction

In lightweight engineering applications the performance of (metal) products depends on their weight, which can be reduced by structural optimization and the use of lightweight alloys like aluminium or titanium. In the Selective Laser Melting (SLM) process, where metal powders are consolidated by selectively laser-scanning the cross-sections of a layered part, both Al alloys and Ti alloys can be processed successfully. Additive manufacturing (AM) processes also enable the manufacturing of very complex shaped parts by offering great "freedom of design", as discussed by Wegener et al. [1]. This important potential can be realized if the process-related limitations are considered carefully. Therefore, design for additive manufacturing, as discussed by Thompson et al. [2] and Vayre et al. [3], is an

important step towards optimizing parts for applications in (e.g.) the space, aerospace and automotive industries.

These industrial sectors, however, require high-quality parts with material properties which are both good and reproducible. However, AM-processes are classified as master forming technologies [4, 5], where the material properties are generated by the manufacturing process itself. Therefore, the alloy chemistry and composition-related behaviour during AM-processing play an important role. Typical AM-process-related effects are the formation of a fine-grained microstructure, with elongated grains growing along the build-up direction of the part. This results in an anisotropy which can reach values >10% in static mechanical properties for many alloys. Examples are Fe-based alloys [6] and Ni-based alloys [7], but also the commonly used 4xxx Al-alloys [8, 9]. In addition to build-up-related anisotropy, further influences are differing processing windows (i.e. different combinations of laser beam properties), laser power, scan speed, layer thickness, and scan strategy. Thijs et al. [10] pointed out that different scan strategies applied to the SLM-processing of AlSi10Mg influences microstructure and texture. They created anisotropic or more isotropic parts by choosing appropriate applied scanning strategies. Siddique et al. [11] analysed the influences of different laser energy inputs, base plate heating and post-process stress relief on the mechanical properties of SLM-processed AlSi12, and revealed significant influences of the applied laser energy density on mechanical properties. Oklami et al. [9] largely support these findings in their review of the potential influences of a variety of processing parameters, such as laser energy input, scan strategy and layer thickness, on densification behaviour, and related microstructural effects sourcing back to the solidification behaviour of the melt-pool during SLM.

Generally, solidification and the emerging microstructure in alloys is driven by the temperature gradient in the melt-pool G and the solidification front growth rate R. According to Ion [12], a high cooling rate $\frac{dT}{dt} = G \cdot R$ promotes higher undercooling, which results in finer grains or finer dendrite arm spacings. The ratio $\frac{\Delta T_0}{D_l}$, with ΔT_0 the solidification temperature range in equilibrium, and D_l the diffusion constant of solute atoms in the melt, drives the solidification morphology. It determines whether a planar solidification front exists, or if it is unstable ($\frac{G}{R} < \frac{\Delta T_0}{D_l}$), giving rise to a more dendritic morphology. From these considerations it becomes clear that the processing conditions in SLM typically have significant effects on the resulting material microstructure, such as grain size distribution and texture, as well as the precipitation behaviour, and consequently on material properties. Such effects are typically driven by the laser energy input used to consolidate the material. In addition, the already consolidated material below the actual layer being built experiences a thermal load generated by temperature peaks which are initiated by the travelling melt pool from subsequent layers being built. This series of temperature peaks is referred to as "intrinsic heat treatment" [13]. It may activate the formation of precipitates in age-hardenable alloys, thereby influencing the mechanical properties of the material.

Therefore, and in order to achieve high-quality metal AM parts with reproducible properties, processing paths must be found which on the one hand minimize solidification-related effects such as the formation

of a textured microstructure, and on the other minimize the influence of different processing windows on mechanical properties. The alloys thus produced would contribute to the improvement of SLM process robustness.

To achieve such properties, several attempts are currently being made using Sc- and Zr-modified Al-Mg alloys. In a recent publication [14] the microstructure formation mechanisms of the Scalmalloy® alloy are discussed. An outstanding property of this alloy system is the formation of a very fine-grained bi-modal grain size distribution, where even the coarser grains are by a factor of 5 to 10 smaller compared to traditional SLM-processed 4xxx alloys. Their excellent mechanical properties are discussed by Palm [15], Schmidke [16] and Spierings et al. [17]. A similar alloy with less Mg (3.4 wt-%) and more Sc (1.08 wt-%) has been analysed Shi et al. [18], completing the densification behaviour at a higher laser powers of 370 W, together with the corresponding hardness properties. Li et al. [19] analysed the properties of an alloy with 6.2 wt-% Mg and a hypo-eutectic Sc- (0.36 wt-%) and Zr- (0.09 wt-%) content, processed at laser powers between 200 W to 400W, and laser scan speeds between 500 mms^{-1} to 1'200 mms^{-1}. They found much larger melt-pools and coarser grains compared to the results presented in [14], along with comparably minor grain-refining effects of the Sc- and Zr-addition. Their TEM analysis showed the existance of large ($\approx$ 100 nm-sized) and small ($\approx$ 5 nm-sized) Al$_3$Sc particles, which they referred to seed crystals for heteogeneous nucleation, and no number- or volume density of such particles was given.

Below we analyse the effects of different laser scan speeds on the resulting mechanical properties in the as-built condition, and analyse the precipitation behaviour of nm-scaled Al$_3$Sc particles during SLM-processing using Transmission Electron Microscopy (TEM).

2 Methods and Materials

2.1 Sample production with SLM

The Scalmalloy® powder material with nominal composition of Al4.6Mg0.66Sc0.42Zr0.49Mn (numbers in wt-%) was used in a ConceptLaser M2 machine equipped with a 200W Gaussian Nd-YAG laser operated in cw mode, with a laser spot diameter of $\approx$ 100 μm (D4σ) [20]. All samples were produced using the maximum laser power P; the slice thickness was 30μm. Further processing parameters were hatch distances d = [135 μm, 150 μm, 165 μm], and laser scan speeds v_s between v_s = 170 mms^{-1} and v_s = 750 mms^{-1}, resulting in a laser energy density-range according to equation (1) of E_V = 54 Jmm^{-3} to E_V = 290 Jmm^{-3} as discussed in Spierings et al. [21].

$$E_V = \frac{P}{d \cdot t \cdot v_s} \tag{1}$$

Hardness testing and microstructural analyses were performed on 10x10x10mm^3 cube samples, whereas static tensile test specimens were produced as cylinders with a length of 80 mm and a diameter of 7 mm in horizontal (90°) and vertical (0°) build orientation. The tensile test samples were machined to the final specimen geometry according to DIN-50'125-A5 with a surface roughness of at least N6 (R_a = 0.8μm) and tested in the as-built condition. For each configuration (build orientation, processing parameter) at least 3 specimens were prepared, except for the samples manufactured with the highest energy input,

where 5 samples were produced. Details of the sample configuration are indicated in the corresponding results section.

2.2 Mechanical characterization

Hardness measurement: The characterization of material hardness was performed using a Gnehm Brickers 220 hardness tester; the results are reported in Brinell hardness (HB) values. A hardness tester, LVD-302 tester, was also used (measuring Vickers hardness and being converted into HB for better comparison). Three to five measurements from differently processed samples were taken from a cross-section in approximately the middle of the sample's height in order to prevent influences from the base-plate alloy composition, and the mean value and one standard deviation were calculated.

Tensile testing: Static mechanical testing was performed on a Walter&Bai hydraulic tensile testing machine LFV-25, equipped with a clip-on axial extensometer type MFA 25 (L_0 = 25mm) for strain measurement. Testing was performed in accordance with EN-10002 / ISO-6892. Using the measured "engineering" stress-strain curves gained from quasi-static tensile testing, the true (index "T"), stress-strain curves and true ultimate strength ($R_{m,T}$) was calculated according to Hosford [22].

2.3 Microstructural analysis

The microstructures were analysed using an FEI Helios 600i dual beam FIB instrument equipped with an EDAX DigiView EBSD system. Analysis was performed on electropolished surfaces, which were prepared using a Struers Tenupol electropolishing unit. The electrolyte (5vol% perchloric acid, 95vol% methanol) was cooled to -50°C and 25volts were applied. Grain size distributions were determined from these EBSD measurements. The largest beam step size used in any measurement was 250 nm (used for very low magnification, large area scans) and when measuring fine grained regions the step size was adjusted to 50 nm or 80nm at x10k magnification to ensure that the average fine grain, e.g. 1 µm in diameter, would still contain > 100 measurements. Hence, the step size was adjusted so that it remained small when compared to the grain size, avoiding stepping over very fine grains. A grain boundary is defined if the misorientation between two points is greater than a maximum allowable misorientation between two points of 5°, and misorientation angles between 1° and 5° were marked as sub-grain boundaries. A grain must, at minimum contain a 2x2 array of points, therefore the minimum grain size using a 50nm step is 100 x 100 nm, anything smaller is ignored.

TEM thin foil specimens of samples manufactured at v_s = 170 mms^{-1} and v_s = 350mms^{-1}, were prepared using identical parameters. Thin foil TEM specimens of samples manufactured at v_s = 200 mm.s^{-1} were prepared using an Ar+-ion mill (GATAN PIPS), and sectioned in the xy-plane. Cutting plane orientations (parallel to the xy-plane or the yz-plane) for microstructural measurements are given in the respective figure captions, using the same coordinate system as in [13]. TEM analysis was performed in a probe side aberration-corrected JEOL 2100FC$_S$ microscope operated at 200kV. Both bright field (BF) and high angle annular dark field (HAADF) images were captured in scanning transmission electron microscopy (STEM) mode. Scattered electrons were collected using a HAADF detector over a semi-angle ranging from 70 – 190 mrad to produce z-sensitive dark field images. Particle size distribution and number

density were determined by manual measurements of particles in TEM and STEM images, and the measurement results are therefore sensitive to imaging conditions, and contrast optimization, as well as to the particles selected. The foil thickness used to calculate number densities was measured using EELS absolute thickness measurements, where the imaged area showed a thickness of $\approx$60nm to $\approx$80nm. For these reasons, and also because of low image contrast, number densities and particle size distribution data must be treated with caution, but can be considered as good estimates.

3 Results

3.1 SLM processing windows

Cube SLM samples, produced with $E_V = 115$ Jmm^{-3}, had a mean density of $99.3 \pm 0.1\%$, whereas the density of samples produced using $E_V \geq 135$ Jmm^{-3} showed a plateau in the mean density at $\approx 99.57 \pm 0.07\%$ (Figure 1). Hence, the further increase in E_V is not the most promising way to maximize the density. The dependence of material density ρ on E_V is shown in Figure 1, and can be described by a mechanical growth model according to equation (2)

$$\rho = c_1 \cdot (1 - c_2 \cdot 10^{-c_3 \cdot Ev}) \tag{2}$$

The fitted parameters using the Euler-method are $c_1 = 0.996 \pm 0.0003$, $c_2 = 0.283 \pm 0.109$ and $c_3 = 0.0497 \pm 0.006$. These data are valid for hatch distances d between 135 μm and 165 μm, and scan speeds from $v_s = 170$ mms^{-1} to $v_s = 750$ mms^{-1}.
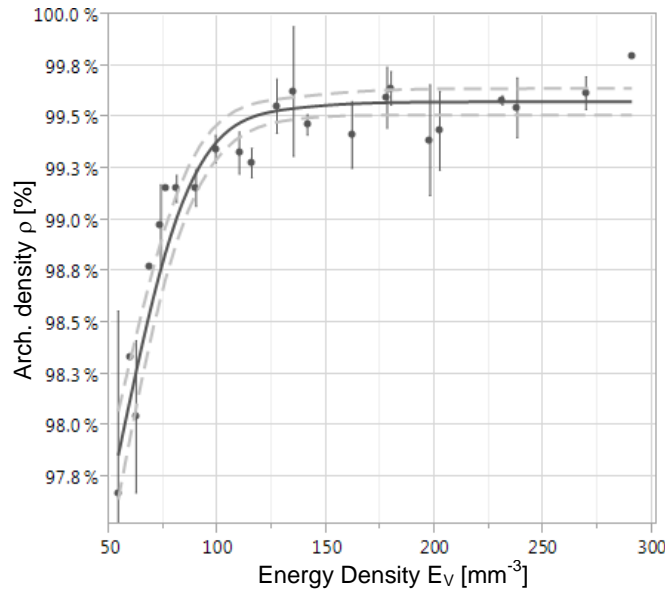

Figure 1: Measured mean density values in dependence on E_V, and the model fit of equation (1) with 95% confidence interval.

It becomes obvious that for a material density of $\geq 99.5\%$ the energy density should be $E_V > 125$ Jmm^{-3}, which corresponds to a scan speed $v_s < 320$ mms^{-1} (for d = 165μm), or $v_s < 395$ mms^{-1} (for d = 135 μm). Consequently, for realization of a density $\geq 99.5\%$ several scan speed and hatch distance combinations are possible. Therefore, as different scan speeds are related to different cooling rates, variations can be expected with regard to the precipitation behaviour. These are discussed in section 3.5.

3.2 Materials hardness

As already mentioned, the "intrinsic heat treatment" may cause the formation of fine dispersed nm-scaled precipitates. Because the precipitation process is temperature- and time-dependent, and thus dependent on the cooling rates and associated laser scan speeds v_s, differences in the initial hardness of the as-processed material can be expected. As shown in Figure 2, a slight increase in hardness is observed for $v_s > 225$ mms^{-1}.
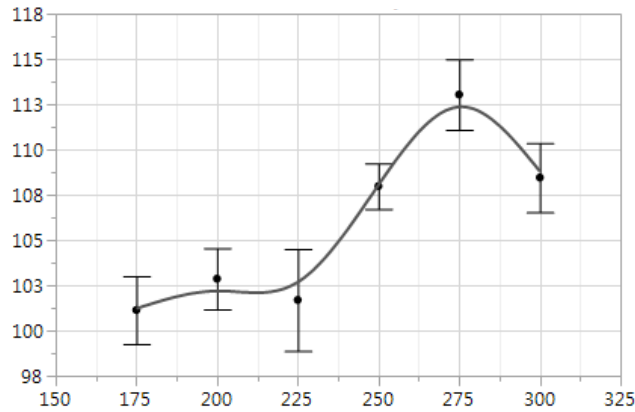

Figure 2: As-processed hardness in dependence on scan speed v_s

3.3 As-processed static mechanical properties

Figure 3 shows static mechanical properties from vertically built samples produced at different scan speeds. Differences in true strengths are marginal, with slightly higher R_m values at lower scan speeds compared to high speeds. Taking the almost identical hardness between $v_s = 170$ mms^{-1} and $v_s = 225$ mms^{-1} and between $v_s = 250$ mms^{-1} and $v_s = 300$ mms^{-1} (Figure 2), the average true ultimate tensile strength for the first three v_s is 422 ± 11 MPa, and 403 ± 14 MPa for the latter, and 415 ± 14 MPa as average over all scan speeds. These slightly better $R_{m,T}$ values at lower scan speeds can be explained by the comparably higher ductility. The average yield strength $R_{P0.2}$ for all scan speeds is 280 ± 6.1 MPa, and the average E-modulus $= 72.9 \pm 3.5$ GPa.
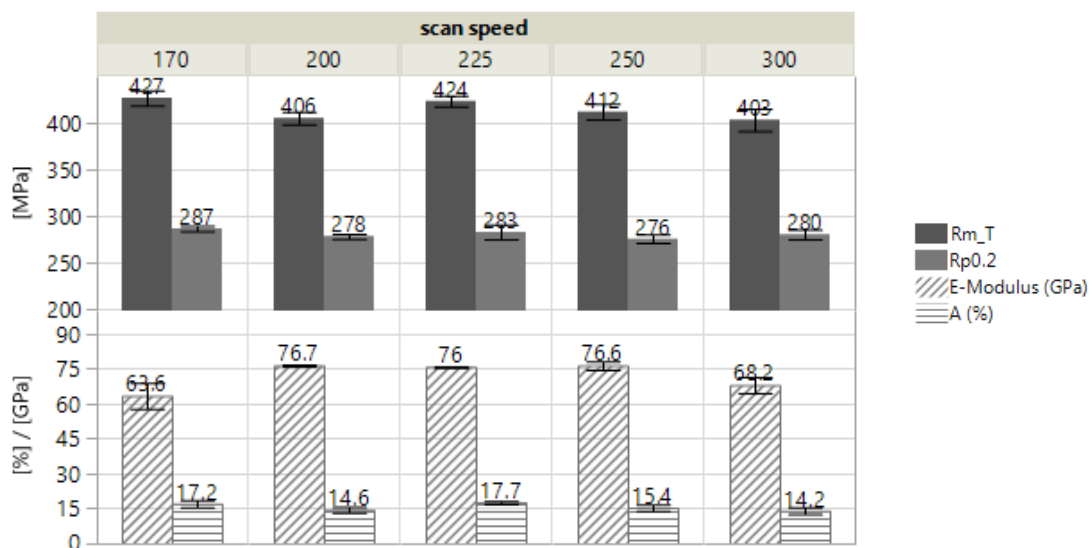

Figure 3: Upper: True ultimate tensile strength $R_{m,T}$ and yield strength $R_{P0.2}$. Lower: E-Modulus and elongation to fracture A_r in the as-processed condition at different scan speeds v_s in vertical build orientation (n = 3). Error-bars indicate the standard deviation.

3.4 As-processed microstructure

Figure 4a and b show the typical bi-modal microstructure of a bi-directionally scanned cube sample manufactured at $v_s = 350 mms^{-1}$, whose formation is discussed in detail in Spierings et al. [14]. Comparison of Figure 4a and d shows that there is almost no difference in appearance between the EBSD scans taken from samples manufactured at $350mms^{-1}$ and $170mms^{-1}$, respectively.
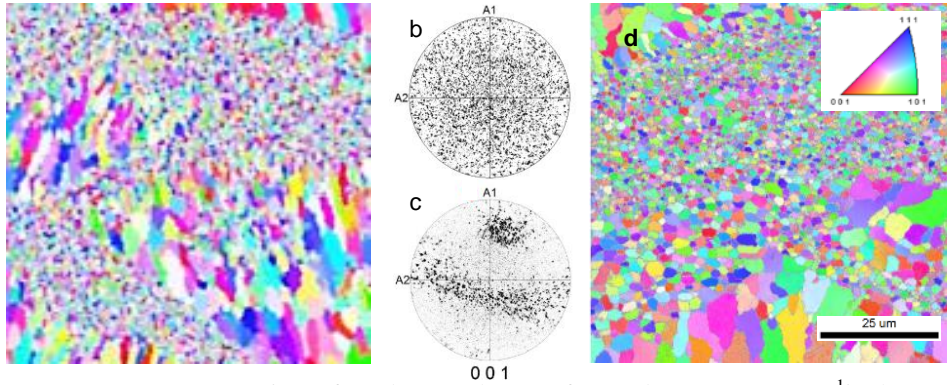

Figure 4: (a) EBSD scan (40nm step size) of a cube sample manufactured at $v_s = 350 mms^{-1}$ in the xz-/yz-plane. b) [001] Pole figure from a fine grained (FG) region and c) [001] Pole figure taken in a coarser grained (CG) region (weighted to grain size). d) EBSD scan of a cube sample manufactured at $v_s = 170 mms^{-1}$, showing a similar bi-modal grain size distribution.

The analysis of the grain size distribution in these two FG and CG regions at both scan speeds is shown in Figure 5. The increase in the scan speed from $v_s = 170 mms^{-1}$ to $v_s = 350 mms^{-1}$ leads, especially in the FG-regions, to a shift in the grain size distribution towards smaller grains. In the FG region the peak grain size at $v_s = 350 mms^{-1}$ is at ≈ 600 nm, whereas at $v_s = 170 mms^{-1}$ this peak is at $\approx 1.14 \mu m$. In the CG region the respective differences are in a similar range, with a peak at $\approx 5 \mu m$ for $v_s = 350 mms^{-1}$, and at $\approx 5.7 \mu m$ for $v_s = 170 mms^{-1}$. These values are not very precise, and can change depending on the specific location analysed. However, Figure 5 shows clearly that the scan speed and hence the energy input does affect the grain size distribution. In the FG regions this grain-size-related change (Hall-Petch) can cause yield strength to increase by $\approx 38\%$ for the higher scan speed, whereas only minimal changes occur in the CG regions. However, these grain-size-related changes in the two regions are overlapped by other strengthening effects, as discussed in section 3.5.
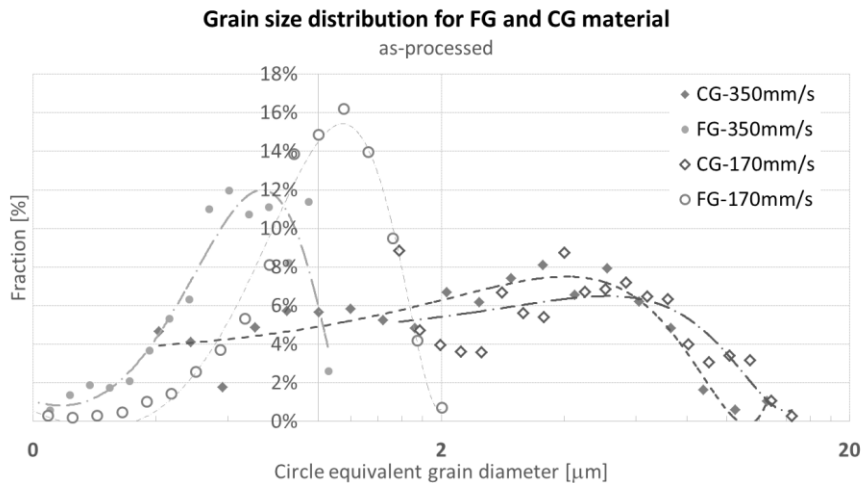

Figure 5: Grain size distribution for coarse- (CG) and fine- (FG) grained material for low ($v_s = 170 mms^{-1}$) and high ($v_s = 300 mms^{-1}$) scan speed samples.

3.5 Precipitates in the as-built condition

3.5.1 Samples manufactured at v_s = 170 mms^{-1}

Figure 6 and Figure 8a show bright field (BF) and dark field (DF) STEM images of material processed at a low scan speed of v_s = 170 mms^{-1}. They reveal that small < 5 nm roughly spherical particles are precipitated, which are identified by the corresponding intensities in the FFT (Figure 6c) as Al$_3$Sc. Figure 8b shows these particles more clearly in the inverse masked FFT image taken from Figure 8a using the Al$_3$Sc-L1$_2$ reflections, underlining the Al$_3$Sc presence. Such Al$_3$Sc particles were found in all the materials processed at this scan speed.

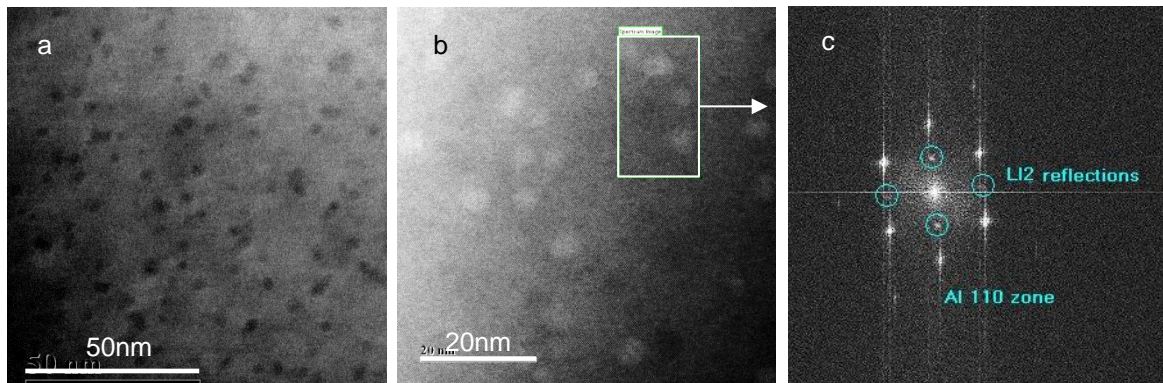**Figure 6:** [110] oriented grain in FG material processed at v_s = 170 mms^{-1}. a) Bright field STEM image b) HR-TEM dark field image showing small < 5nm Al$_3$Sc particles. c) FFT image from b showing L1$_2$ reflections of Al matrix and Al$_3$Sc particles

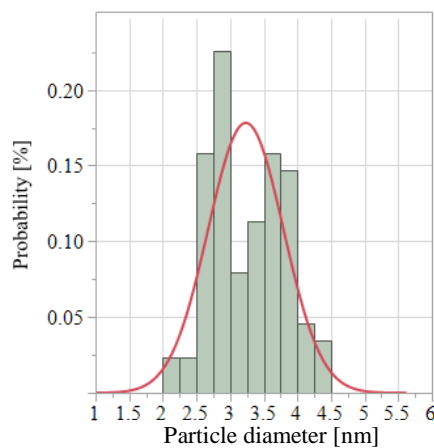Figure 7 shows the particle size distribution, with mean particle diameters of 3.2 ± 0.56 nm.

Figure 7: Al$_3$Sc particle size distribution with Normal distribution fit for as-built sample manufactured at v_s = 170mms^{-1}. Particle diameters are estimated by manual selection of particles.

Figure 8c is a magnification of an Al$_3$Sc particle. It looks like two particles with different compositions next to each other: possibly an Al$_3$Sc particle next to an Al-Mg oxide, although the specific composition was not identified. However, this would be reasonable as it would confirm the particle formation routes discussed in Spierings [14].
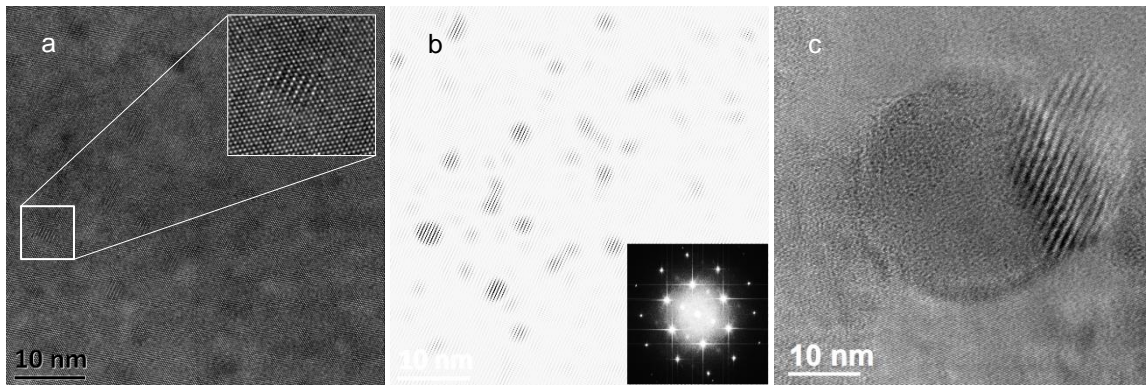
Figure 8: [110] oriented grain in FG material processed at $v_s = 170 \ mms^{-1}$. a) High resolution DF-TEM image with small Al_3Sc particles shown in the insert. b) Inverse masked FFT image of a) using the Al_3Sc-$L1_2$ reflections indicated in the insert, showing the Al_3Sc particles (optimized for better contrast). c) Two spherical particles in an FG [211] grain, possibly an Al_3Sc next to Al-Mg oxides.

Next to intragranular particles, further particles are found at grain boundaries. A fine $\approx$ 10 nm to 20 nm Al_3Sc particle located at the grain boundary of an [110] oriented grain is shown in Figure 9a. Figure 9b is a HAADF-STEM image of an Al_3Sc particle at the grain boundary, whose crystal structure has been identified by the FFT shown in the imprint by the required reflections.
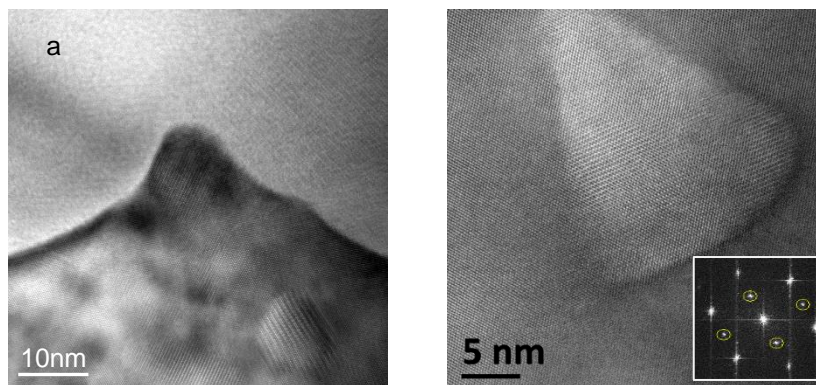

Figure 9: a) Grain boundary particle in a [110] oriented grain ($v_s = 170 \ mms^{-1}$). b) HAADF-STEM at higher resolution of a GB- Al_3Sc particle, identified by the $L1_2$ reflections in the corresponding FFT (insert).

3.5.2 Samples manufactured at $v_s = 200 \ mms^{-1}$

Figure 10 reveals the results of the EDX analysis of a coarse-grained region. It shows the elemental distribution of the most important elements, with mainly grain boundary particles of varying composition. Most of them are Al-Mg oxides, partially with traces of Fe, Si and Mn, whereas Sc- and Zr-rich particles are found both at grain boundaries and intragranular (see also Spierings et al [14]). Some larger Al-Mg-oxides are found, predominately located at grain boundaries, with the largest sizes being $\approx$ 350 nm.
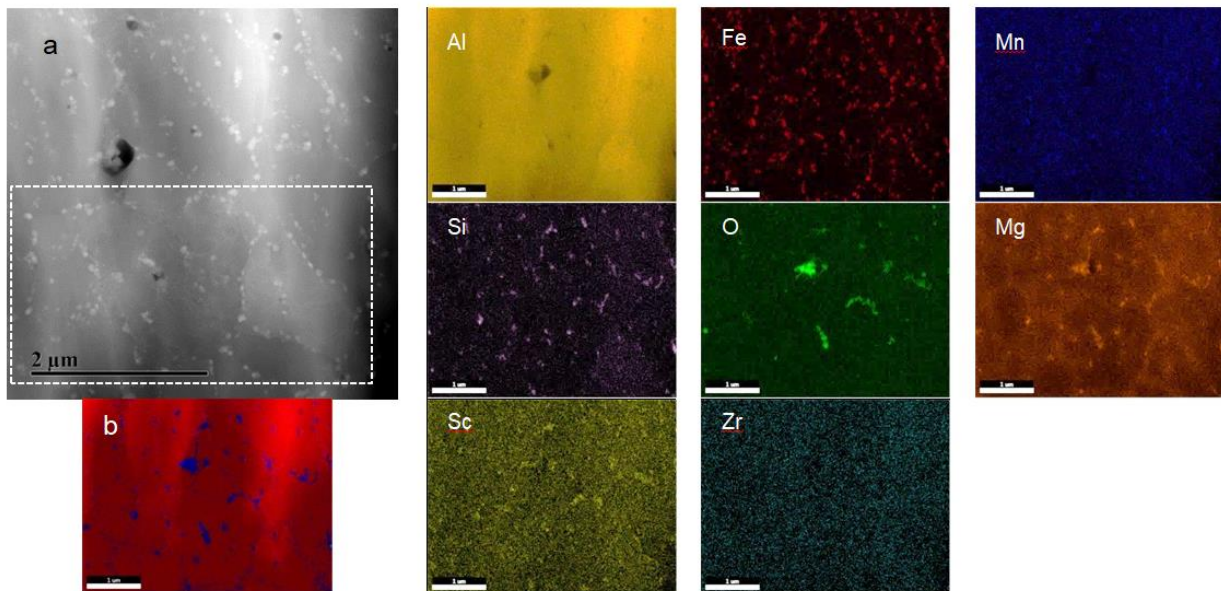
Figure 10: a) DF-STEM image of coarse-grained region of material processed at $v_s = 170$ mms^{-1}. b) Shows the local area-/volume-related distribution of Al (92%) and other mixed particles (8%). EDX mapping for the most important elements (improved for brightness and contrast), with scale bars $= 1\mu m$.

Figure 11a is a BF-TEM image taken from the same area as shown in Figure 10a (indicated by the dashed box), showing two grains with an ideal orientation for visualizing dislocations. Their presence indicates the occurrence of high shrinkage-related stresses which are induced during the cooling down of the material, as is typical in laser processing. Figure 11b presents grains imaged in the fine-grained region. In such FG regions no signs of high dislocation density were found, in contrast to the CG regions. However, the darker contrast of grains in this image shows the contrast sensitivity of grain orientation during TEM. This importance of grain orientation, also in identifying precipitates, becomes obvious in Figure 11c, which shows a grain boundary triple-point with no signs of precipitation in the left-hand grain. The features shown in the other two grains on zone are unidentified, but could be any type of Al$_3$Sc precipitate.
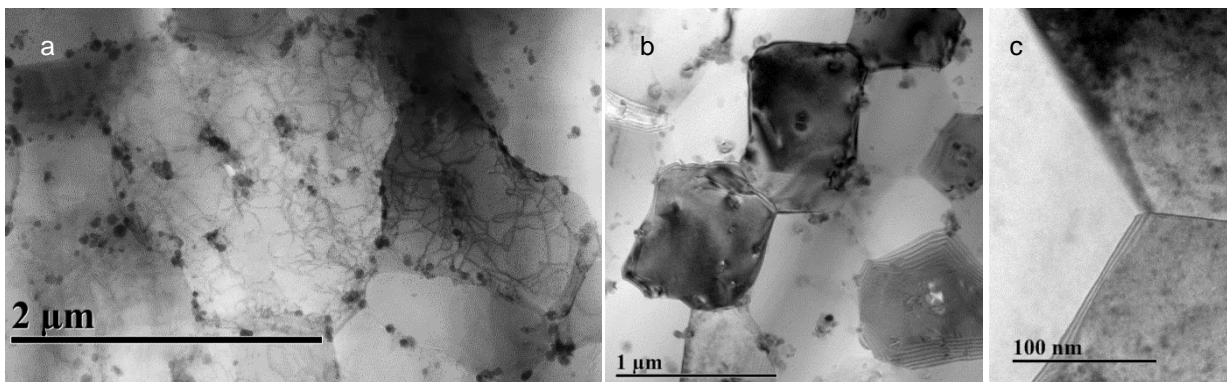

Figure 11: a) Low magnification BF-TEM images of a xy-section in a CG region processed at $v_s = 200$ mms^{-1}, showing relatively high dislocation density. b) FG region with no signs of increased dislocation density. c) Triple grain boundary with an absence of precipitation, probably due to unfavourable grain orientation.

3.5.3 Samples manufactured at $v_s = 250$ mms^{-1} and $v_s = 350$ mms^{-1}

The results seen at higher scan speeds of $v_s = 250$ mms^{-1} and $v_s = 350$mms^{-1} are similar to those at $v_s = 200$ mms^{-1}. Figure 12a is a STEM image of a fine grain processed at $v_s = 250$ mms^{-1}, and Figure 12b of a coarse grain at $v_s = 350$ mms^{-1}, with FFT inserts showing no evidence of Al$_3$Sc.
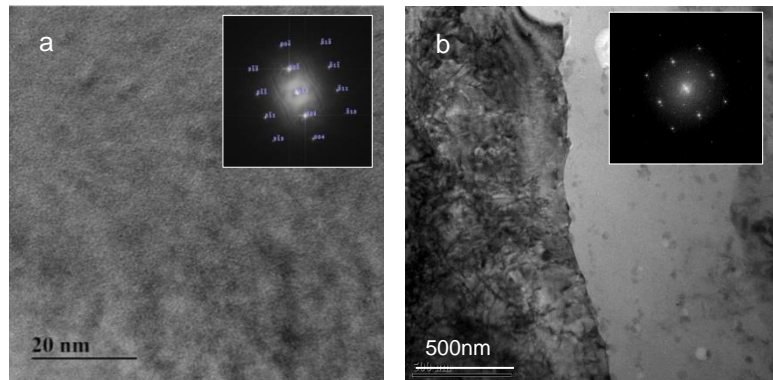

Figure 12: a) STEM image of Ar$^+$-milled samples produced at $v_s = 250$mms^{-1} in the fine-grained region on a [001] zone axis. b) TEM images of an electro-polished foil processed at $v_s = 350$mms^{-1} in the coarse-grained region, and heavily dislocated grain on the left-hand side. Imprints represent the corresponding FFT images.

In all TEM images from different grains analysed at different orientations ([001], [011], [113]), no evidence of intragranular Al$_3$Sc precipitation was found. The only FFT-Al$_3$Sc reflections found in as-built material is from larger, approximately 50nm seed crystals, as discussed in [14]. As also shown in Figure 11a, the coarse grains in particular are heavily dislocated (Figure 12b, Figure 13a), whereas many fewer dislocations were found in the fine-grained area. Figure 13b is a representation of a fine grain with some dislocations, and internal ≈ 50 nm sized particles.
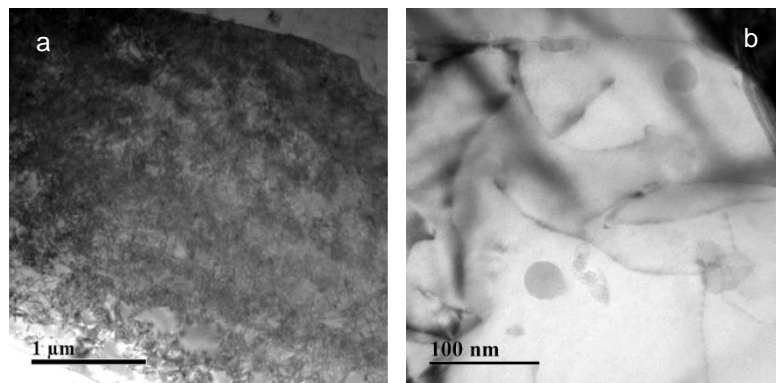

Figure 13: TEM images of an electro-polished foil processed at $v_s = 350$mms^{-1}.a) Heavily dislocated columnar grain region. b) Fine-grained area at higher magnification showing particles and only a few dislocations.

4 Discussion

It has been shown that different processing parameters can be used to consolidate the material to almost full density, reaching > 99.5%. Due to the high thermal conductivity of aluminium, the required optimal hatch distances are ≈ 35 % to 65 % larger than the laser spot diameter. Figure 1 shows that for this given range of hatch distances, the material density is mainly driven by the applied laser energy density E_V. An optimal range for E_V is $\approx [125, 150]$ Jmm^{-3}, reaching ≥ 99.5 % material density. This E_V-range is higher

compared to the results presented by Shi et al. [18], who suggested an optimal range at high laser power of $E_V = [77, 103]$ Jmm^{-3}, enabling then much higher scan speeds compared to this work.

The material's microstructure, and hence the share between coarse- and fine-grained material, is almost unaffected by the various laser energy inputs or laser scan speeds, respectively. The most important differences are only found in the change in the grain size distributions in the FG regions, with smaller grains at higher scan speeds. However, although the peak grain size is reduced by increasing scan speed from $\approx$ 1.1 µm to $\approx$ 600 nm, this grain structure still has to be considered as very fine if compared to traditional alloys, or to the CG regions. This type of microstructure is a direct effect of microstructure formation mechanisms where a high density of relatively coarse, 50 nm- to 100 nm-sized Al$_3$Sc seed crystals is responsible for the fine-grained area, and where they dissolve due to high temperatures in the coarse-grained material, as discussed by Spierings et al. [14]. The smaller peak grain size at $v_s = 350$ mms^{-1} is a result of the approximately doubled cooling rates at this scan speed, compared to $v_s = 170$ mms^{-1}, which is a well-known driver for smaller grain sizes in homogeneous nucleation. Therefore, from a microstructural point of view structural and mechanical anisotropy is not affected by the specific processing parameters used.

Next to Al$_3$Sc seed crystals, many grain boundary particles exist, predominantly (but not exclusively) in the fine-grained area. These include 10 nm- to 20 nm-sized Al$_3$Sc (Figure 9), and other mixed particles with Fe, Mn and Si and Al-Mg oxides, as found from EDX scans (Figure 10), and are similar to the particles precipitated at $v_s = 170$ mms^{-1} as discussed in Spierings [14]. They stabilize the microstructure against different levels of heat input (various scan speeds and the intrinsic heat treatments form subsequent layers being built), and are therefore also responsible for maintaining the similar grain size distributions from low ($v_s = 170$ mms^{-1}) to high ($v_s = 350$ mms^{-1}) scan speeds (Figure 5). In contrast, most of the Sc and Zr remains homogeneously distributed in the material (Figure 10), either as particles or in solid solution, and enable post-process age hardening.

However, there are varying levels of precipitation of < 5nm-sized particles in dependence on the scan speed used to manufacture the specimens (from $v_s = 170$ mms^{-1} to $v_s = 350$ mms^{-1}). In summary, in as-processed Sc- and Zr-containing Al-Mg alloy, < 5nm, spherical, coherent Al$_3$Sc particles were only found at low scan speeds of $v_s = 170$ mms^{-1}. The particle number densities estimated depend on the specific region and the real foil thickness (between 60 nm to 80 nm), but are in the range of $N_V \approx 5 \cdot 10^{22}$ m^{-3} to $1 \cdot 10^{23}$ m^{-3}. These Al$_3$Sc particles can be formed during solidification of the alloy if the cooling rate is not too high, as is the case at lower scan speeds, or by the "intrinsic heat treatment", i.e. the cyclic heat input from subsequent layers being built, as discussed by Jägle [13]. Actually, the time periods where higher temperatures are available are significantly longer at $v_s = 170$ mms^{-1} than at e.g. $v_s = 350$ mms^{-1}, as is shown in Figure 14 using the simulation model discussed in Heeling et al. [23] and Spierings et al. [14]. In this figure, 13 different reference points are selected in the cross-section of the melt-pool (Figure 14a), and the corresponding time-temperature profiles are shown in Figure 14b.
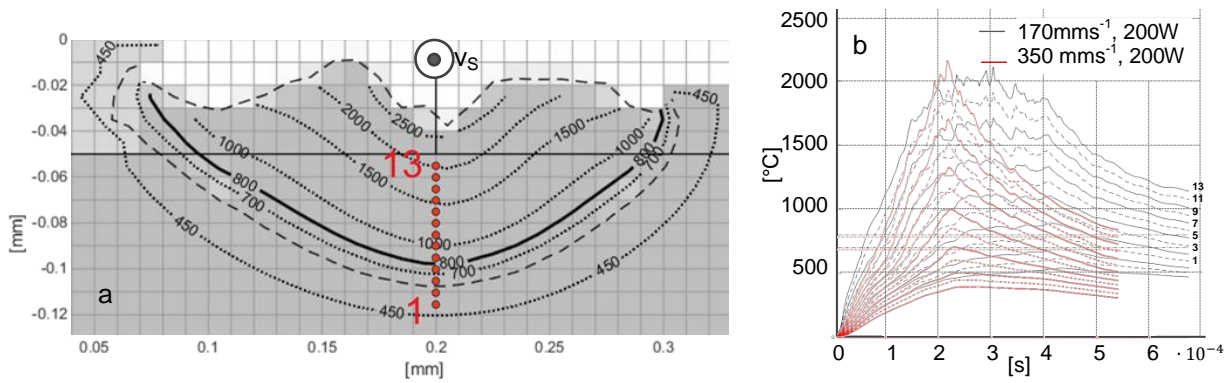
Figure 14: a) Simulated cross-section of a melt-pool at $v_s = 170 mms^{-1}$, with 13 reference points in its centre. b) Simulated time-temperature dependence at these 13 different positions in the melt-pool at $v_s = 170 mms^{-1}$ and $v_s = 350 mms^{-1}$.

The model reveals that both the time to the maximal temperature and the maximal temperature itself show almost no dependence on the scan speed, but that the cooling rates between these two scan speeds are significantly different ($\approx 1.55 \cdot 10^6 Ks^{-1}$ versus $0.76 \cdot 10^6 Ks^{-1}$). It follows that these differences influence the continuous precipitation behaviour of Al_3Sc particles, where the higher cooling rates at scan speeds $v_s > 200 mms^{-1}$ are responsible for the lack of any Al_3Sc particles. At such high speeds no Al_3Sc particles were found in any of the TEM analyses performed on fine- and coarse-grained material, which was confirmed by the lack of Al_3Sc reflections in the selected area diffraction patterns and FFT image reconstructions. Consequently, the precipitation behaviour of < 5 nm sized $Al_3(Sc_x Zr_{1-x})$ particles is mainly driven by the laser scan speed and/or the intrinsic heat treatment from subsequent layers being built (and related cooling rates). Any effect of different hatch distances on the number density of such precipitates is expected to be low as for instance a smaller hatch distance would only slightly increase the additional total intrinsic heat input from neighbouring scan tracks. Hence, at higher scan speeds, a Sc and Zr supersaturated matrix is formed and only a subsequent post-process heat treatment result in the precipitation of nm-scaled intragranular Al_3Sc. These results are basically in-line with the findings of Shi et al. [18] who also stated a reduced as-fabricated solute supersaturation at higher heat input.

All these effects together account for the overall material hardness with a slight increase of < 10% for higher scan speeds (Figure 2). Initially one would expect that the existence of Al_3Sc particles should increase hardness to above the values for particle-free material. However, different strengthening mechanisms are responsible for the final hardness and mechanical properties, including precipitation hardening, the high dislocation density (especially in the coarse-grained regions), and solution hardening of solute Sc and Zr atoms. Grain size hardening also plays a role, but because the fraction of fine- to coarse-grained material remains more or less unaffected by the scan speed, and because the Hall-Petch factor for aluminium is comparably small [24], no significant differences in grain size hardening for the different scan speeds is expected. Therefore, and due to the different levels of contribution to hardness by the different effects, it is difficult, if not impossible, to differentiate between the specific contributions.

The simultaneous complex interactions between the various interlinked strengthening mechanisms mean that their individual effects remain inextricable. However, from an engineering point of view, the differences in mechanical properties (Figure 3) appear to be minor, and hence the flexibility of the

processing window allows the design of parts independent of anisotropy or part orientation during the SLM build process.

5 Conclusions

The advantageous evolution of fine-grained microstructures in the Al-Mg-Sc-Zr alloy system, when produced by conventional processing routes such as casting, are already well documented. Recently it was shown clearly that this alloy system is also very advantageous in additive processing using SLM, where a basically fine-grained, bi-modal microstructure evolves at all processing conditions used. The fine-grained area-fraction is formed due to the existence of a high number density of Al_3Sc seed crystals with a size of up to ≈ 100 nm, and the microstructure is stabilized against grain growth by grain boundary precipitation of various particles, including ≈ 20 nm-sized coherent Al_3Sc particles, and further features including Fe, Mn, Si and Al-Mg oxides. Consequently, the grain size distributions in the fine- and coarse-grained regions are only very slightly dependent on the laser energy density, where even at high energy input the small grains remain $< 2\mu m$, without any preferential grain orientation, which is an important contrast to other SLM-processed conventional casting (4xxx) alloys. However, a dependence on laser scan speed for the precipitation of nm-scaled particles is observed where at lower scan speeds < 5nm intragranular, coherent Al_3Sc particles form at a high number density, because the energy input during processing or by the intrinsic heat treatment from subsequent layers being built, respectively, is sufficient to continuously precipitate these particles. In contrast, at higher scan speeds no intragranular particles of this size are observed, and a higher fractoin of Sc remains in super-saturated solid solution.

Overall, the superimposition of the multiple strengthening mechanisms, which are related to various precipitates and lattice defects, generates only slight hardness- and mechanical properties-dependence on the scan speed. The yield strength is practically unaffected by the laser scan speed, whereas true strengh slightly tends to somewhat lower values at higher scan speeds as it would be ecpected. However, the differences are comparably low, and can also be affected by a potential local impact of remaining porosity. For more a more precise analysis of mechanical data, a separate analyse with more test samples per condition would be required. However, the observed general behaviour is advantageous for engineering purposes because it underlines that there is no unfavourable dependence of material properties on processing parameters. These results therefore demonstrate the significance of alloy composition in achieving robust processing conditions.

Where the productivity of the SLM process is to be optimized, high laser scan speeds are hence advantageous and not detrimental from a microstructural point of view. Post-process heat treatment retains full potential for precipitating fine dispersed coherent Al_3Sc or $Al_3(Sc_x Zr_{1-x})$ particles. This is of great relevance for the processing and the final product, and represents an exceptional quality advantage of this alloy system.

Manuscript

6 Acknowledgements

Literature

[1] K. Wegener, A.B. Spierings, M. Schmid, Additive Manufacturing on the Way to industrialization, in: T.O. Dimiter Dimitrov (Ed.) 6. Int. Conf. on Competitive Manufacturing, Stellenbosch, ZA, 2016, p. 12.

[2] M.K. Thompson, G. Moroni, T. Vaneker, G. Fadel, R.I. Campbell, I. Gibson, A. Bernard, J. Schulz, P. Graf, B. Ahuja, F. Martina, Design for Additive Manufacturing: Trends, opportunities, considerations, and constraints, CIRP Annals - Manufacturing Technology 65(2) (2016) 737-760.

[3] B. Vayre, F. Vignat, F. Villeneuve, Identification on Some Design Key Parameters for Additive Manufacturing: Application on Electron Beam Melting, Procedia CIRP 7(0) (2013) 264-269.

[4] ISO, ISO 17296-1:2014(en) Additive manufacturing —General principles — Part 1: Terminology, 2014, p. 26.

[5] ISO, ISO 17296-2:2015(en) Additive manufacturing —General principles — Part 2: Overview of process categories and feedstock, 2015.

[6] A.B. Spierings, N. Herres, G. Levy, Influence of the particle size distribution on surface quality and mechanical properties in additive manufactured stainless steel parts, Rapid Prototyping Journal 17(3) (2011) 195 - 202.

[7] T. Bauer, K. Dawson, A.B. Spierings, K. Wegener, Microstructure and mechanical characterisation of SLM processed Haynes 230®, in: D.L. Bourell (Ed.) Proceedings of the Annual International Solid Freeform Fabrication Symposium, Austin, Texas, 2015.

[8] D. Buchbinder, W. Meiners, K. Wissenbach, R. Propawe, Selective Laser Melting of Aluminium Die-Cast Alloy, Fraunhofer Direct Digital Manufacturing Conference 2014, Demmer, A., Berlin, Germany, 2014, p. 6.

[9] E.O. Olakanmi, R.F. Cochrane, K.W. Dalgarno, A review on selective laser sintering/melting (SLS/SLM) of aluminium alloy powders: Processing, microstructure, and properties, Prog. Mater. Sci. 74 (2015) 401-477.

[10] L. Thijs, K. Kempen, J.-P. Kruth, J. Van Humbeeck, Fine-structured aluminium products with controllable texture by selective laser melting of pre-alloyed AlSi10Mg powder, Acta Materialia 61(5) (2013) 1809-1819.

[11] S. Siddique, M. Imran, E. Wycisk, C. Emmelmann, F. Walther, Influence of process-induced microstructure and imperfections on mechanical properties of AlSi12 processed by selective laser melting, J. Mater. Process. Technol. 221 (2015) 205-213.

[12] J. Ion, Laser Processing of Engineering Materials, Elsevier, Oxford, 2005.

[13] E.A. Jägle, Z. Sheng, L. Wu, L. Lu, J. Risse, A. Weisheit, D. Raabe, Precipitation Reactions in Age-Hardenable Alloys During Laser Additive Manufacturing, JOM - Journal of the Minerals, Metals & Materials Society (2016) 1-7.

[14] A.B. Spierings, K. Dawson, T. Heeling, P.J. Uggowitzer, R. Schäublin, F. Palm, K. Wegener, Microstructural features of Sc- and Zr-modified Al-Mg alloys processed by selective laser melting, Materials & Design 115 (2017) 52-63.

[15] F. Palm, K. Schmidtke, Exceptional Grain Refinement in Directly Built Up Sc-Modified AlMg Allboys is Promising a Quantum Leap in Ultimate Light Weight Design, Proceedings of the 9th International Conference Trends in Welding Research, Chicago 2012.

[16] K. Schmidtke, F. Palm, A. Hawkins, C. Emmelmann, Process and Mechanical Properties: Applicability of a Scandium modified Al-alloy for Laser Additive Manufacturing, Phys. Procedia 12(Part 1) (2011) 369-374.

[17] A.B. Spierings, K. Dawson, K. Kern, F. Palm, K. Wegener, SLM-processed Sc- and Zr-modified Al-Mg alloy: Mechanical properties and microstructural effects of heat-treatment, Materials Science & Engineering A 701 (2017) 264-273.

[18] Y. Shi, P. Rometsch, K. Yang, F. Palm, X. Wu, Characterisation of a novel Sc and Zr modified Al–Mg alloy fabricated by selective laser melting, Materials Letters 196(Supplement C) (2017) 347-350.

[19] R. Li, M. Wang, T. Yuan, B. Song, C. Chen, K. Zhou, P. Cao, Selective laser melting of a novel Sc and Zr modified Al-6.2Mg alloy: Processing, microstructure, and properties, Powder Technology 319(Supplement C) (2017) 117-128.

[20] M. Cloots, P.J. Uggowitzer, K. Wegener, Investigations on the microstructure and crack formation of IN738LC samples processed by selective laser melting using Gaussian and doughnut profiles, Materials & Design 89 (2016) 770-784.

[21] A.B. Spierings, K. Dawson, M. Voegtlin, F. Palm, P.J. Uggowitzer, Microstructure and mechanical properties of as-processed Scandium-modified aluminium using Selective Laser Melting, CIRP Ann. Manuf. Technol. 65(1) (2016) 213-216.

[22] W.F. Hosford, Mechanical Behavior of Materials, Cambridge University Press, New York, 2005.

[23] T. Heeling, K. Wegener, Computational Investigation of Synchronized Multibeam Strategies for the Selective Laser Melting Process, Physics Procedia 83 (2016) 899-908.

[24] S. Thangaraju, M. Heilmaier, B.S. Murty, S.S. Vadlamani, On the Estimation of True Hall–Petch Constants and Their Role on the Superposition Law Exponent in Al Alloys, Advanced Engineering Materials 14(10) (2012) 892-897.